








PAPER

[View Article Online](#)
[View Journal](#) | [View Issue](#)Cite this: *Dalton Trans.*, 2024, **53**,
3254Spin canting and slow magnetic relaxation in
mononuclear cobalt(II) sulfadiazine ternary
complexes†Cristian Villa-Pérez, ^{*a} Andoni Zabala-Lekuona, ^{*b}
Iñigo J. Vitorica-Yrezabal, ^c José Manuel Seco, ^b Javier Cepeda, ^b
Gustavo Alberto Echeverría ^d and Delia Beatriz Soria ^{*a}

Monomeric [Co(SDZ)₂phen] (**1**) and [Co(SDZ)(bq)Cl] (**2**) complexes (SDZ = sulfadiazine, phen = 1,10-phenanthroline, and bq = 2,2'-biquinoline) have been synthesized and characterized. X-ray diffraction studies indicate that SDZ acts as a bidentate ligand coordinating through the sulfonamide and the pyrimidine N atoms in both compounds. In complex **1**, the coordination sphere consists of two SDZ ligands and a bis-chelating phen ligand, giving rise to a CoN₆ coordination sphere. On the other hand, **2** has a CoN₄Cl core, with two N-atoms from SDZ and two from the bq ligand. Both compounds have been studied by dc and ac magnetometry and shown to display slow magnetic relaxation under an optimum external dc field (1 kOe) at low temperatures. Moreover, compound **2** displays long range magnetic ordering provided by spin-canted antiferromagnetism, which has been characterized by further field-dependent magnetic susceptibility measurements, FC/ZFC curves, hysteresis loops and frequency-independent ac curves. The signs of the calculated *D* parameters, positive in **1** and negative in **2**, have been rationalized according to the two lowest-lying transitions in the orbital energy diagrams derived from *ab initio* ligand field theory (AFLT). In a subsequent attempt to reveal the possible hidden zero-field SMM behaviour, Ni(II)-based **3** and Co(II)-doped Ni(II)-based (with a Ni : Co ratio of 0.9 : 0.1) heterometallic compound **2**_{Ni} were synthesized.

Received 24th July 2023,
Accepted 3rd January 2024
DOI: 10.1039/d3dt02359arsc.li/dalton

Introduction

Single-molecule magnets (SMMs) are compounds that show slow relaxation of magnetization and magnetic hysteresis below a certain temperature (*T*_B, blocking temperature). The slow magnetic relaxation behaviour is associated with an energy barrier (*U*) originating from large anisotropy (*D* or axial zero-field splitting, *zfs*, a parameter for 3d ions) in ions with a high-spin ground-state (*S*).¹ The earliest efforts in the search of compounds with larger energy barriers were dedicated to the

development of polynuclear complexes with a large total spin by increasing the number of coupled paramagnetic centres. However, the control of the magnetic anisotropy axes in polynuclear systems is complicated, and in many cases, the increase of *S* led to a significant diminution of the magnetic anisotropy with subsequent poor SMM properties.² In light of this, molecules with a single anisotropic paramagnetic centre that meet the essential criteria for observing slow magnetic relaxation were discovered and called single-ion magnets (SIMs) or mononuclear SMMs.³ After the discovery of Ln(III) based SIMs, a remarkable number of studies involving mononuclear 4f based materials have been reported.⁴ However, 3d row transition metals are still of great interest in the field of molecular magnetism and, thus, several studies on different ions (Cr(II)/(III), Mn(III), Fe(I)/(II), Co(II) and Ni(I)/(II)) have been conducted over the last few years.^{5–21} Although large energy barrier values have been observed in transition-metal based SIMs (as high as *U*_{eff} = 450 cm^{−1} for a Co(II) linear complex¹⁸), further studies are necessary in order to reach the final goal of operating temperatures closer to room temperature, in other words, open hysteresis loops at high temperatures.

Co(II)-based complexes are good candidates for the development of SMMs due to their large magnetic anisotropy, which originates from a strong contribution of first-order spin-orbit

^aCEQUINOR (CONICET, CCT – La Plata), Departamento de Química, Facultad de Ciencias Exactas, Universidad Nacional de la Plata, Bv. 120 no. 1465, 1900 La Plata, Argentina. E-mail: cristianvilla@quimica.unlp.edu.ar, soria@quimica.unlp.edu.ar

^bDepartamento de Química Aplicada, Facultad de Química, Universidad del País Vasco/Euskal Herriko Unibertsitatea (UPV/EHU), Paseo Manuel Lardizabal no. 3, 20018 Donostia, Spain. E-mail: andoni.zabala@ehu.es

^cDepartamento de Química Inorgánica, Facultad de Ciencias, Universidad de Granada, 18071 Granada, Spain

^dIFLP (CONICET, CCT – La Plata), Departamento de Física, Facultad de Ciencias Exactas, Universidad Nacional de la Plata, 47 y 115, 1900 La Plata, Argentina

†Electronic supplementary information (ESI) available. CCDC 2040162 (**1**), 2040161 (**2**) and 2309444 (**3**). For ESI and crystallographic data in CIF or other electronic format see DOI: <https://doi.org/10.1039/d3dt02359a>

coupling to the total magnetic moment. The magnetic properties of these complexes are strongly influenced by the coordination environment provided by the ligands, and there is a great interest in developing complexes with coordination numbers as low as possible, due to their expected large magnetic anisotropy.¹⁷ High coordination numbers are known to suppress the orbital contribution (L , orbital angular momentum) and subsequent magnetic anisotropy. Indeed, the ground-state could be appropriately described by the spin (S) term. When low coordination numbers are obtained, the d orbitals fall within narrower energy ranges, simulating $4f$ orbitals of lanthanide compounds. For instance, the current and previous records of the largest barriers to the reversal of magnetization in transition metal complexes are two linear Co(II) complexes.^{17,18} Nevertheless, it has also been proved that compounds with higher coordination numbers could have significant magnetic anisotropy. Several Co(II) single-ion magnets with coordination numbers ranging from 2 to 8 and with diverse geometries have been reported so far.^{17–20,22–27} Hence, selecting appropriate ligands for the development of suitable ligand fields is fundamental, as they will modulate the magnetic anisotropy of the metal ion and, therefore, the potential SMM/SIM behaviour.

In this work, we report novel complexes that are derivatives of the sulfadiazine ligand, which is a widely used antibiotic in both human and veterinary medicine. In addition, it has several coordination modes that could lead to a wide variety of materials.²⁸ Note that we planned this research project as a continuation of a previously published work reported by some of us, in which two sulfadiazine six-coordinated Co(II) complexes with the ancillary ligands 2,2'-bipyridine and 6-methoxyquinoline were described.²² Both compounds had been shown to be field-induced SMMs with U_{eff} values of 50.6 K (2,2'-bipyridine derivative) and 13.7 K (6-methoxyquinoline derivative). In the present case, the heterocyclic compounds 1,10'-phenanthroline and 2,2'-biquinoline have been used as ancillary ligands. The former one could provide a similar structure to the one studied with 2,2'-bipyridine, while the latter one was selected as a bulkier ligand with the aim of sterically hindering some coordinating positions and, thus, for obtaining lower coordination numbers.

The present work covers the synthesis and characterization of three novel compounds, followed by experimental and theoretical magnetic studies.

Experimental

Synthetic procedures

Chemicals. All chemicals were of reagent grade and were used as commercially obtained without any further purification.

Synthesis of [Co(SDZ)₂phen] (1). 25 mL of a methanolic solution containing NaSDZ (1 mmol) and 1,10-phenanthroline (0.5 mmol) was added dropwise to 25 mL of a CoCl₂·6H₂O solution (0.5 mmol, MeOH) under continuous stirring at room

temperature. After 1 h, the complex was filtered to obtain an orange powder, and the filtrate was left for slow evaporation. After a few days, orange single crystals were recovered and used for the structural determination by XRD measurements. The elemental analysis (EA) gave the following results for CoC₃₂H₂₆N₁₀O₄S₂ (PM: 737.68): experimental (calculated): C, 51.71 (52.10); H, 3.49 (3.55); N, 18.70 (18.99); S, 8.94 (8.68)%. The reaction yield was 87.6%.

Synthesis of [TM(SDZ)(bq)Cl] (TM = Co for 2; TM = Ni for 3). 0.5 mmol of NaSDZ, 0.5 mmol of 2,2'-biquinoline, and 30 mL of an ethanol/methanol mixture (5 : 1) were placed in a two-necked round bottom flask provided with a condenser and a dropping funnel. The system was heated to reflux and after the complete dissolution of the ligands, an ethanolic solution of the corresponding metal chloride (0.5 mmol, 10 mL) was dropwise added from the funnel. The reflux was maintained under continuous stirring for 1 h. During the reaction, the compound was obtained as a green powder, which was hot filtered and washed with ethanol. The filtrate was preserved for slow evaporation, and after a few days, green crystals were obtained and used for structural determination in the case of 2. Single crystals of 3 were obtained by recrystallization in ethanol. The EA gave the following results for CoC₂₈H₂₁N₆O₂SCl (PM: 599.96): experimental (calculated): C, 56.09 (56.05); H, 3.34 (3.53); N, 13.65 (14.01); S, 5.31 (5.34)%; NiC₂₈H₂₁N₆O₂SCl (PM: 599.72): experimental (calculated): C, 56.17 (56.08); H, 3.31 (3.53); N, 13.84 (14.01); S, 5.41 (5.35)%. The reaction yields were 82.2 and 79.6% for 2 and 3, respectively.

Synthesis of [Co_{0.1}Ni_{0.9}(SDZ)(bq)Cl] (2_{Ni}). The synthesis of the doped compound 2_{Ni} was carried out following the same procedure described for 2 and 3, but using a 1 : 10 Co : Ni ratio. Note that this is a routinely employed method usually used to dilute transition metal and lanthanide based SMMs in diamagnetic Zn(II) and Y(III) matrices, respectively.^{29,30} The phase purity of the material was confirmed by PXRD (Fig. S2†). The stoichiometry of the material was determined by ICP-MS, which confirmed the Co : Ni ratio of 1 : 9 in the material.

Physical measurements

Elemental analyses (C, H, N, and S) were performed using a Leco CHNS-932 microanalyzer. Magnetic susceptibility measurements were carried out on polycrystalline samples of the complexes using a Quantum Design SQUID MPMS-7T susceptometer at applied magnetic fields indicated in the static magnetic properties section. The susceptibility data were corrected for the diamagnetism estimated from Pascal's tables, the temperature-independent paramagnetism, and the magnetization of the sample holder. Alternating current measurements were performed using a physical property measurement System-Quantum Design model 6000 magnetometer under a 3.5 G ac field and at frequencies ranging from 60 to 10 000 Hz.

ICP-MS analysis

Around 20 mg of the sample was treated with concentrated HNO₃ in a closed vessel of PFA (Saville®) and was heated at 100 °C for 24 hours. The solution was diluted (1 : 55 000) for



the determination of the analytes. All masses were measured using a balance weighing with an accuracy of ± 0.0001 g to avoid errors related to volumetric dilution. The analyses were carried out following a previously reported protocol³¹ with slight modification using a Thermo Fisher XSeriesII quadrupole ICPMS. The calibration was made using a 10 ppm multielemental solution (PerkinElmer with traceability to NIST standards). A rhodium based solution was used as an internal standard. Quality control solutions (QCS) were repeatedly measured to ensure the quality of the results.

X-ray diffraction data collection and structure determination

Data for the complexes were recorded using a Rigaku-Oxford Gemini diffractometer equipped with an EOS CCD detector (for compounds **1** and **2**) or a Bruker VENTURE area detector (for compound **3**), both of which are equipped with graphite-monochromated Mo-K α ($\lambda = 0.71073$ Å) radiation. X-ray diffraction intensities were collected (ω -scans with θ - and κ -offsets), integrated, and scaled with the CrysAlisPro³² suite of programs. The unit-cell parameters were obtained through least-squares refinement (based on the angular settings for all collected reflections with intensities larger than seven times the standard deviation of measurement errors). The data were empirically corrected for absorption employing the multi-scan method implemented in CrysAlisPro. The structures were solved by direct methods using SHELXS-97,³³ and the molecular models were refined using the full-matrix least-squares procedure on F^2 with SHELXL-97.³⁴ All atoms except for the amino H-atoms were positioned stereochemically and refined using the riding model, with their displacement parameter set equal to 1.2 times the equivalent isotropic displacement parameter of the bonded carbon atoms. On the other hand, the amino H-atoms were located in a difference Fourier map phased on the heavier atoms and refined with the N-H and H...H distances restrained to the target values of 0.86(1) and 1.49(1) Å, respectively, with their displacement parameters set equal to 1.5 times the equivalent isotropic displacement parameter of the corresponding nitrogen atom.

The crystal data and refinement results are summarized in Table S1.† CCDC 2040162, 2040161 and 2309444 for **1**–**3**,† respectively, contain the supplementary crystallographic data for this paper.

The X-ray powder diffraction (XRPD) patterns were recorded over powdered samples (Fig. S1 and S2†). For data acquisition, a Philips X'PERT powder diffractometer was used with Cu-K α radiation ($\lambda = 1.5418$ Å) covering the range of $5 < 2\theta < 50^\circ$ with a step size of 0.026° and an acquisition time of 2.5 s per step at 25 °C.

Computational details

A Gaussian 16 package³⁵ was employed for partially (hydrogen positions) optimizing the excerpts of all compounds taken from the X-ray structures. These calculations were performed using DFT with the UB3LYP functional³⁶ employing the TZV basis set for the metal atoms³⁷ and the 6-31G** basis set for the remaining non-metal atoms.³⁸ *Ab initio* calculations were

implemented in ORCA (version 5.0.3)^{39,40} to estimate zfs parameters on aforementioned models. These single point calculations were conducted with the B3LYP functional^{41,42} using the def2-TZVP basis sets for all atoms and def2-QZVPP for the metal atoms, recontracted for the zeroth-order regular approximation (ZORA) relativistic correction.^{43–46} RIJCOSX approximation with appropriate auxiliary basis sets (def2/J)⁴⁵ was employed for all calculations. Calculations using the state-average complete active space self-consistent field (SA-CASSCF) method were performed incorporating the five d-orbitals and seven (for **1** and **2**) and eight electrons (for **3**). Ten quartets and forty doublets for the Co(II)-based compounds and ten triplets and ten singlets for the Ni(II)-based compounds were included.⁴⁷ NEVPT2 calculations were performed on SA-CASSCF converged wave functions to take in account the dynamic correlation,⁴⁸ a strategy successfully used earlier to obtain accurate estimations of the zfs parameters.^{47,49}

Results and discussion

The reaction between NaSDZ, an additional chelating ligand and CoCl₂·6H₂O in alcoholic solutions gives rise to two mononuclear compounds with variable coordination geometry. Hence, they both display distinct static and dynamic magnetic properties arising from either bulk or single ion sources.

Structural description of compounds [Co(SDZ)₂phen] (**1**) and [Co(SDZ)(bq)Cl] (**2**)

Complexes **1** and **2** crystallize in the orthorhombic *Pac*2₁ and monoclinic *P*2₁/*n* space groups, respectively, both with 4 molecules per unit cell. Note that the description of **3** has been omitted due to the fact that it is isostructural to **2**. Fig. 1 shows the coordination sphere of the Co(II) cations bonded to the ligands together with the used labels. In **1**, the Co(II) ion displays a CoN₆ coordination sphere, whereas **2** has a CoN₄Cl environment. The SHAPE software was used for the calculation of the degree of distortion of the coordination polyhedra with respect to ideal geometries.⁵⁰ The results revealed that the geometry around the metal in **1** is close in shape to an octahedron (TPR-6), while **2** is closer to a square pyramid (SPY-5) when compared with ideal six and five vertex polyhedra, respectively (see Tables S2 and S3 in the ESI†). Notably, both coordination environments are far from ideal polyhedra according to the large SHAPE values.

The coordination geometry distortion can be evidenced by the bond distances and angles in the coordination spheres (see Table S4†). For **1**, the coordination sphere around the Co(II) ion consists of the phen nitrogen atoms at 2.102(7) and 2.113(5) Å and four N-atoms from two SDZ molecules at 2.106(4), 2.193(5), 2.276(5) and 2.094(5) Å, completing a distorted octahedral geometry. All bonding angles deviate from the ideal values. For instance, both SDZ ligands bond to the metal ion through the sulfonamido and one pyrimidine nitrogen atoms, establishing four-membered CoNCN' rings with N–Co–N' che-



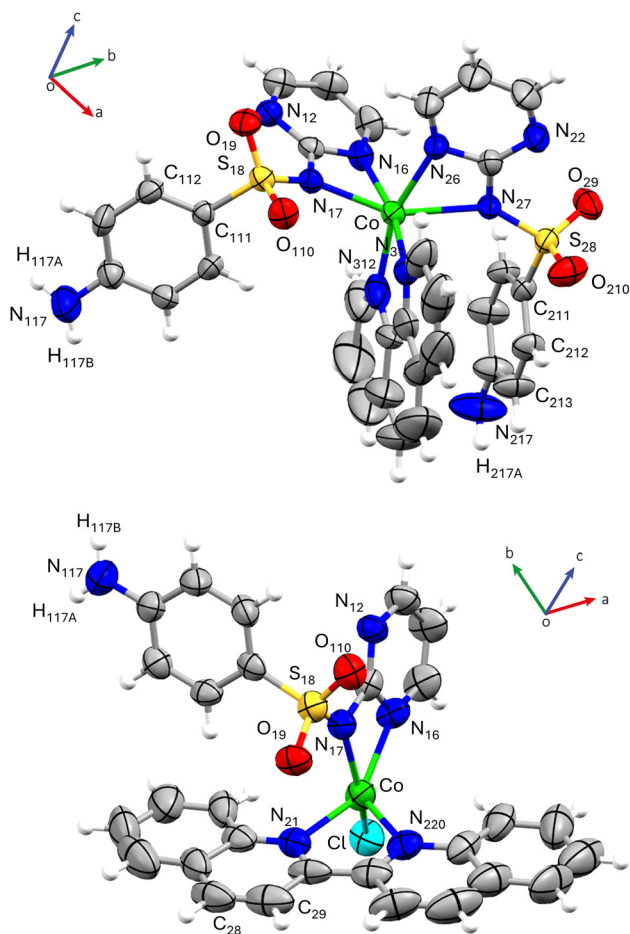


Fig. 1 Crystal structures of complexes **1** (top) and **2** (bottom). Co(II) ion, and carbon, oxygen, nitrogen, sulphur, chloride and hydrogen atoms are shown by green, grey, red, blue, yellow, turquoise and white ORTEP ellipsoids (50% probability), respectively.

lating angles of 60.88° and 62.48° . On the other hand, the phen ligand chelates the metal ion forming an angle of 78.41° .

In **2**, the cation is surrounded by a distorted square pyramidal environment. The equatorial positions are occupied by a chlorine atom at $2.2746(2)$ Å, two nitrogen atoms from an SDZ ligand at $2.1166(2)$ and $2.1735(2)$ Å, and another one from bq at $2.061(4)$ Å. The apical position of the pyramid is occupied by the second N-atom of the bq at $2.039(5)$ Å. Co(II) is located 0.405 Å above the base of the distorted square pyramid. The angles in the pyramidal base are deviated from the ideal 90° , with values ranging from 61.87° (N16–Co–N17) to 99.43° (Cl1–Co–N16). Similarly, the angles between the base atoms and the apical N220 deviate from the ideal value, with values as low as 79.67° (N21–Co–N220) and as high as 119.01° (N16–Co–N220).

Furthermore, the crystal lattices are stabilized because of the presence of several intermolecular hydrogen bonds (Table S5[†]). In both complexes, the main intermolecular interactions, which stabilize the crystal structure, are the N–H \cdots O hydrogen bonds connecting the anilinic SDZ nitrogen atom to the sulfonamide oxygen atoms, generating an extended struc-

tural pattern. In addition, $\pi\cdots\pi$ intermolecular interactions also play an important role in the molecular packing of compound **2** as detailed below (Fig. S3[†]).

In **1**, the amino nitrogen and oxygen atoms of neighboring SDZ ligands, symmetry-related by the c and a -glide planes, are involved in four N–H \cdots O hydrogen bonds, forming a 3D N–H \cdots O hydrogen bonding network that is spread along the three crystallographic directions (Fig. 2). In addition, the supramolecular crystal building is further stabilized by weaker C–H \cdots N and C–H \cdots O hydrogen bonds involving carbon atoms of the phenylamine group and pyrimidine nitrogen or sulfonamide oxygen atoms. Among all intermolecular pathways, the shortest Co \cdots Co distances are of $8.773(1)$ Å in **1**.

In **2**, the crystal building involves various types of interactions of variable nature and strength that set the neighbouring complexes at different distances between Co(II) centres. The main interaction between the complexes is due to the formation of dimeric units through relatively strong $\pi\cdots\pi$ interactions (given the large overlap between the central aromatic rings of bq ligands with C \cdots C distances in the 3.5 – 3.7 Å range; see Table S6[†] for further details) and weaker C211–H211 \cdots Cl1 hydrogen bonds. This can be denoted as a centrosymmetric interaction pathway due to the presence of an inversion center that places the stacked bq ligands at *ca.* 3.57 Å between the centroids of interacting aromatic rings (see Fig. S3[†]). Interestingly, within these layers, bq ligands are packed in a fashion that resembles the herringbone packing of polycyclic aromatic hydrocarbons.^{51,52} As a consequence, the Co(II) ions of neighbouring complexes are situated at a distance of 7.2 Å, which is the shortest intermolecular pathway connecting the metal atoms. Moreover, each of the complexes of the centrosymmetric dimers establishes C–H \cdots π interactions among SDZ ligands in addition to C221–H221 \cdots Cl1 (involving the aromatic bq carbon atom) weaker bonds to gene-

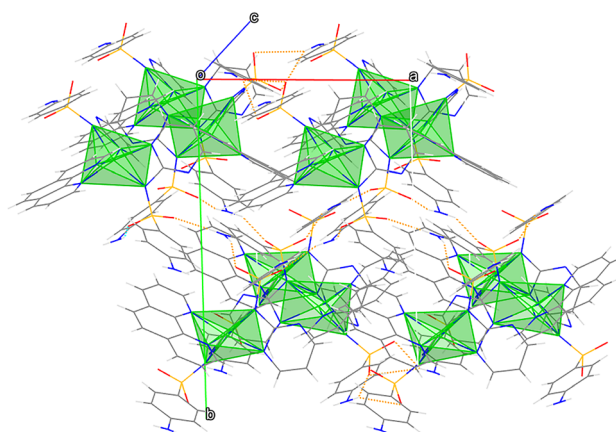


Fig. 2 Extended unit cell content of compound **1** showing the 3D N–H \cdots O hydrogen bonding network. Co(II) ion, and carbon, oxygen, nitrogen and sulphur atoms are shown in green, grey, red, blue and yellow, respectively. For clarity, the Co(II) coordination sphere and N–H \cdots O hydrogen bonds are shown as polyhedra and orange dashed lines, respectively.

rate infinite arrays of complexes along the crystallographic a axis, resulting in complexes being separated by a Co...Co distance of 9.3 Å. As a result of both interaction pathways, 2D layers arranged along the (101) plane are formed (Fig. 3).

Additionally, note that arrays of $\pi\cdots\pi$ stacked dimers are further linked with each other through additional $\pi\cdots\pi$ interactions between the peripheral aromatic rings of bq ligands (Fig. S3†). Finally, the 2D layers are further piled up along the

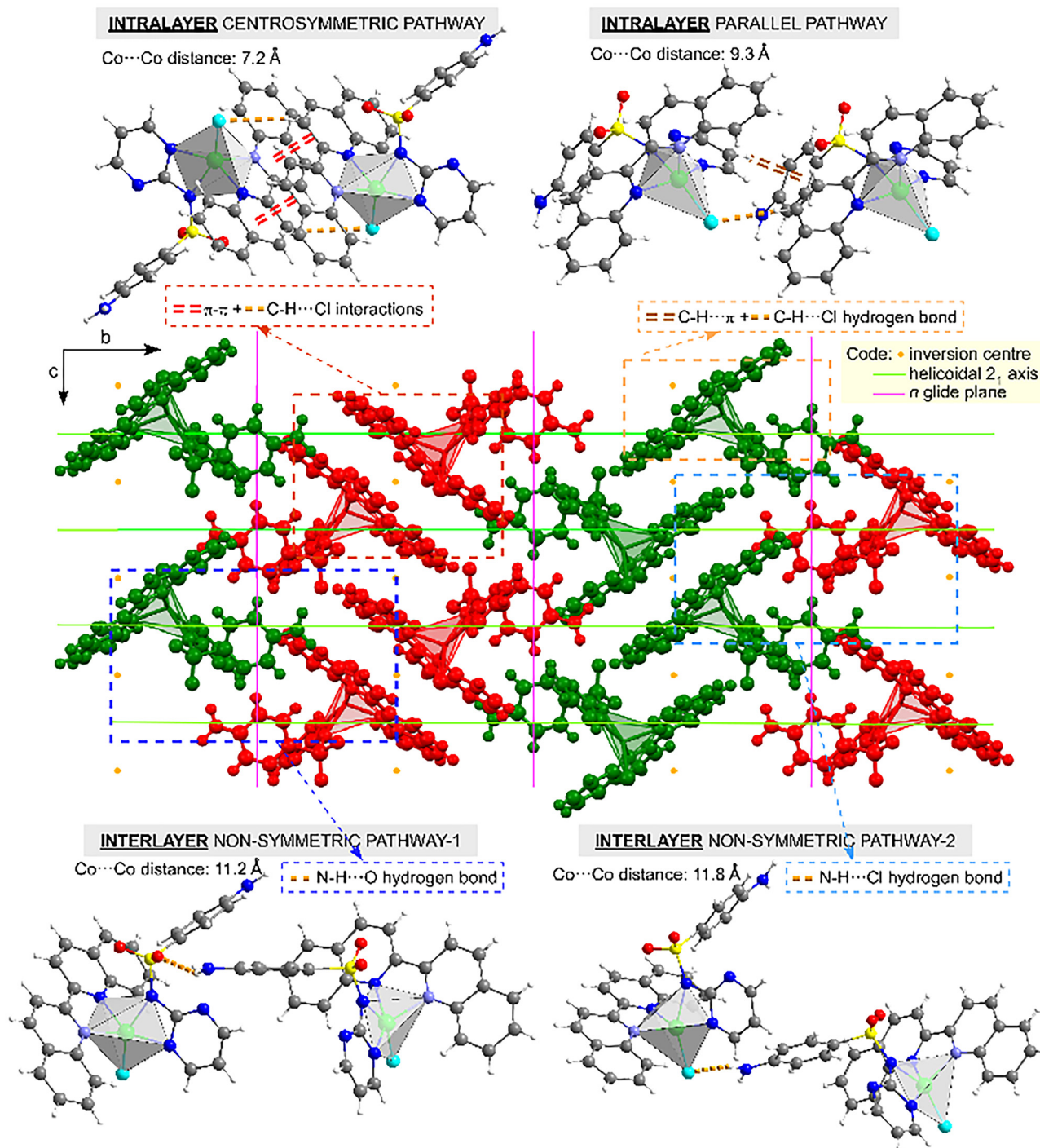


Fig. 3 View of the crystal packing (central image) of compound 2 showing the symmetry elements along the [1 0 0] axis showing the arrangement of complexes into 2D layers (in the ac plane) and their sequential arrangement (layers successively in green and red colours). The most relevant intermolecular interactions connecting the complexes with their respective Co...Co distances (to account for the plausible superexchange pathways) are also shown. Note that both $\pi\cdots\pi$ stackings between bq ligands and N-H...O/C-H...Cl/N-H...Cl hydrogen bonds between SDZ ligands are displayed.



crystallographic *b* axis in such a way that dimeric entities are displayed alternately with two alternative orientations with respect to the piling direction, given that neighbouring layers are related by the glide *n* plane. As a result, two inequivalent additional intermolecular pathways are observed between complexes pertaining to alternate layers: (i) a non-symmetric pathway involving the N117–H117A...O110 hydrogen bond established between the amino nitrogen and sulfonamido oxygen atoms of two neighboring SDZ (imposing a Co...Co distance of 11.2 Å) and (ii) a non-symmetric pathway along the N117–H117B...Cl1 hydrogen bond established by the amino nitrogen atom of the SDZ ligand (imposing a Co...Co distance of 11.9 Å). Most importantly, these two superexchange pathways share the absence of a symmetry element between the complexes, and their relative orientation obeys to restrictions of the overall packing, in such a way that pyramidal environments are relatively twisted showing non-fully parallel nor anti-parallel orientations (to give an orientative measure, angles between Cu–N_{apical} vectors are of 59.3° and 82.3° for the non-symmetric pathways 1 and 2, respectively).

Static magnetic properties

Variable-temperature (2–300 K) dependence of the magnetic susceptibility data was analysed over polycrystalline samples of 1–3 under a dc applied field of 1 kOe.

For **1**, the room temperature $\chi_{\text{M}}T$ product of 2.84 cm³ mol^{−1} K is significantly higher than the expected spin-only value for an octahedral Co(II) ion (1.87 cm³ mol^{−1} K with *g* = 2.01), which suggests the presence of certain spin–orbit coupling (Fig. 4). On cooling down, the $\chi_{\text{M}}T$ value remains almost constant before a final and more abrupt drop below 75 K, reaching a minimum value of 1.68 cm³ mol^{−1} K at 2 K. This progressive decrease may be attributed to the first-order SOC effect as sizeable antiferromagnetic interactions have been ruled out in view of the long distances between spin carriers in the structure (the shortest interactions impose Co...Co distances of *ca.*

8.7 Å) and, most importantly, the absence of remarkable π – π or hydrogen bonding interactions to mediate magnetic exchange. On account of the CoN₆ distorted octahedron present in compound **1**, the potential magnetic anisotropy usually observed in these metal centres⁵³ was further corroborated by isothermal magnetization curves collected in the 2–5 K range (Fig. 4, inset), as they do not reach the theoretical saturation for an *S* = 3/2 system (*M*_{sat} = 3.3 μ_{B} , with *g* = 2.2).

In order to evaluate the sign and magnitude of the zfs parameter, we simultaneously fitted both the susceptibility and magnetization data with the spin Hamiltonian shown in eqn (1) using the PHI program:⁵⁴

$$\hat{H} = D \left(\hat{S}_z^2 - \frac{S(S+1)}{3} \right) + E (\hat{S}_x^2 - \hat{S}_y^2) + \mu_{\text{B}} H g \hat{S} \quad (1)$$

where *S* corresponds to the spin (*S* = 3/2), *D* and *E* account for the axial and rhombic magnetic anisotropies, respectively, and *H* is the applied magnetic field. The best fit provided the following set of parameters: *D* = +45.4 cm^{−1}, *E*/*D* = 0.33, *g* = 2.43, TIP = 2 × 10^{−4} and *R* = 3.8 × 10^{−4}. It must be noted that a similar result (with a slightly worse goodness of fit) could be obtained by changing the sign of *D*, which is not surprising given the large rhombicity estimated from the fitting (*E*/*D* = 0.33), which makes the sign of the main *D* parameter completely meaningless as largely discussed in several works.^{55–57} *Ab initio* multireference calculations on a suitable model of **1** based on the X-ray coordinates overestimate the experimental result, but give a positive and almost axial zfs parameter (*D* = +70.1 cm^{−1} and *E*/*D* = 0.08; see Fig. S6 and Table S7†). According to the CASSCF calculation, the ground electronic state corresponds to the (d_{xz})²(d_{yz})²(d_{xy})¹(d_{z²})¹(d_{x²−y²})¹ configuration (see Fig. S4 and Tables S9, S10†). These values, in line with those commonly observed for octahedral Co(II) ions,^{47,58,59} although clearly overestimated compared to experimental ones, confirm the suitability of the aforementioned fitting.

The temperature dependence of the $\chi_{\text{M}}T$ product for compound **2** notably differs from **1**, especially at the lowest temperatures (Fig. 5). At room temperature, the $\chi_{\text{M}}T$ value of 3.41 cm³ mol^{−1} K is much higher than the expected spin-only value for a Co(II) ion. On cooling down, this value smoothly decreases, reaching a minimum value of 3.17 cm³ mol^{−1} K at 46 K, and then abruptly increases up to 6.34 cm³ mol^{−1} K, describing a maximum at 11 K, eventually dropping to 2.26 cm³ mol^{−1} K at 2 K. This behaviour is indicative of a weak net ferromagnetic ordering in the compound, which is quite surprising in view of the molecular nature of the compound composed of isolated complexes. Nonetheless, the relatively short intermolecular Co...Co distances imposed by π ... π interactions between 2,2′-biquinoline ligands combined with other weak couplings along non-symmetric pathways in the structure seem to be responsible for the observed long-range ferromagnetic coupling (see Fig. S5†).

The occurrence of canted antiferromagnetism was further confirmed by several additional measurements. On the one

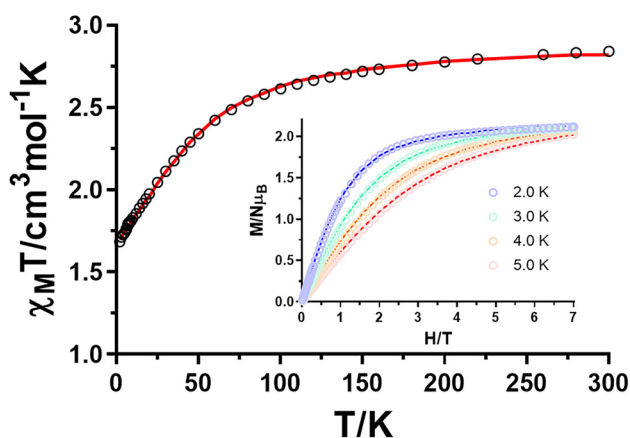


Fig. 4 Variable-temperature dc magnetic susceptibility data for **1** collected under a 1 kOe applied dc field. Inset: The variable-field magnetization curves recorded in the 2–5 K temperature range. The continuous lines in both plots represent fits to eqn (1) using the PHI program.



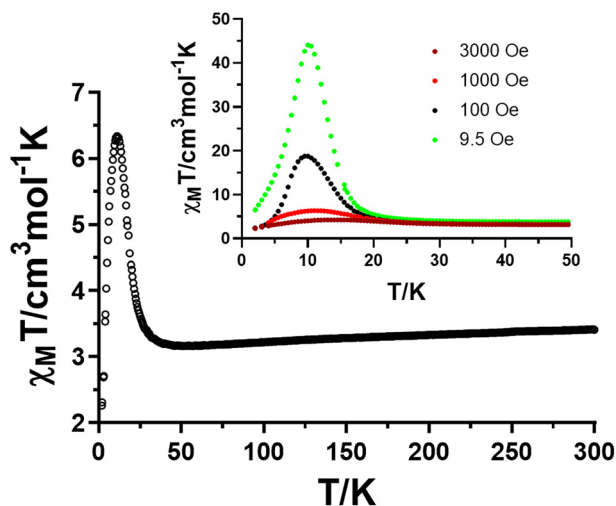


Fig. 5 Variable-temperature dc magnetic susceptibility data for **2** collected under a 1 kOe applied dc field. Inset: $\chi_M T$ plots recorded under different external magnetic fields.

hand, the susceptibility curves measured at variable fields reveal a strong field-dependent response (Fig. 5, inset), which agrees with the usual behaviour observed for ferromagnetic compounds. Moreover, field-cooled (FC) and zero-field-cooled (ZFC) χ_M curves show a clear bifurcation at 11 K (Fig. 6, top), which fits with the temperature at which frequency-independent maxima are observed in the ac dynamic magnetic measurements (*vide infra*). Lastly, isothermal magnetic hysteresis loops were recorded in the 2–5 K temperature range, displaying a noticeable opening at all studied temperatures (Fig. 6, bottom). The S-shaped curves observed at the highest measured temperatures (4–5 K) are specially worth mentioning, where a large positive slope at almost zero applied fields ($H_{dc} < 0.1$ T) is followed by a lower slope at higher fields. This shape, quite smoothed in the present case due to the weak magnetic interactions (*vide infra*), is indicative of a change in the regime of the magnetic ordering, in line with canted ferromagnetic behaviour. Furthermore, at 2 K remnant magnetization and coercive field values of $0.06\mu_B$ and 315 Oe were measured, respectively. According to eqn (2), a small canting angle of 1.44° was estimated (M_R and M_S stand for the remnant and saturation magnetization values, respectively):

$$\psi = \tan^{-1}\left(\frac{M_R}{M_S}\right) \quad (2)$$

Considering that complex **2** does not crystallize in a non-centrosymmetric space group, we assume that the spin-canting behaviour arises from the single-ion magnetic anisotropy of Co (II) ions and the relative dispositions between adjacent complexes in the structure, forced by intermolecular Co...Co interactions, although there could be some superexchange pathway allowing for substantial antisymmetric exchange. In particular, the present structure is characterized by multiple intermolecular pathways along the spin carriers (take into account that intermolecular pathways in Fig. 3 represent all potential

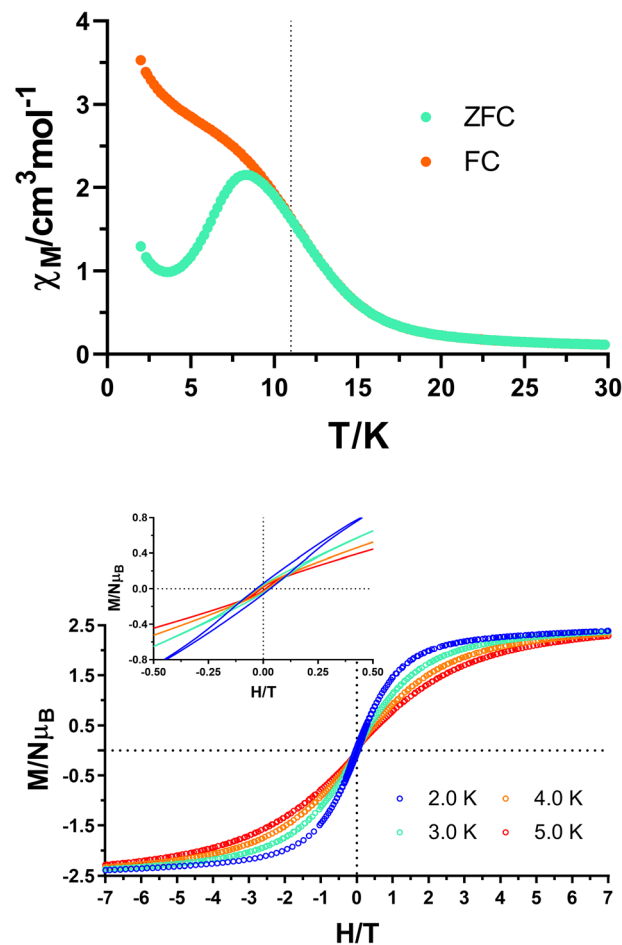


Fig. 6 For **2**, temperature-dependent ZFC and FC molar susceptibility curves in the low temperature region (top) and magnetic hysteresis loops recorded in the 2–5 K temperature range (bottom).

magnetic couplings), all of which are expected to result in very weak exchange interactions. Note, in this sense, that no reliable calculations could be performed to provide the magnitude of the exchange coupling through the exchange pathways owing to the limitations of DFT to estimate the value of J constant in these kinds of superexchange pathways.⁶⁰ In principle, the strongest magnetic interaction should come from the so-called intralayer centrosymmetric pathway occurring through the $\pi\cdots\pi$ stacking between bq ligands because (i) it brings the shortest Co...Co intermolecular distance (7.2 Å) in the structure and (ii) the spin density is relatively large over the bq ligand (Fig. S5†). As reported in previous works, π - π interactions are known to yield weak ferromagnetic couplings,^{61,62} which seems to be the case of the present compound in view of the structural characteristics of the interacting bq ligands (see Table S6†). Assuming that this interaction is the strongest one along the 2D planes (drawn in red and green in Fig. 3), there would be a net ferromagnetic ordering in the layers given the weaker superexchange couplings occurring through the remaining bridges within the layers. Hereafter, assuming that weak antiferromagnetic interactions may occur along the inter-



layer non-symmetric pathways (involving Co...Co of *ca.* 11 Å, see bottom of Fig. 3), the magnetic moment of the 2D layers should not be fully cancelled with each other when packed along the crystallographic *b* axis. In fact, a representation of the *D*-tensor frame in two Co centres interacting through this large pathway shows how magnetic axes are not fully parallel, but canted to each other, and thus, given the absence of symmetry elements different from *n* glide planes, uncompensated magnetic moments along the packing direction (*b* axis) lead to the observed spin-canting behavior (Fig. S9†). Taking into account that this explanation cannot be fully supported by calculations (in view of the impossibility to reliably calculate *J* constants), another possible explanation would suppose that interactions along the interlayer non-symmetric pathways are the main superexchange bridges governing the magnetic properties (canting the spins between individual complexes at low temperature), which is *a priori* more difficult to understand in view of the long Co...Co distances and low spin density present over the interacting atoms. In any case, the presence of the observed canting (involving S-shaped hysteresis curves) is well explained according to these two exchange pathways containing Co ions related by *n* glide planes, in which antisymmetric exchange could be non-zero. As an illustrative example, we would like to cite the research work reported by Zhang *et al.*, in which they compared several one-dimensional Co(II) based compounds.⁶³ As they state, the coordination spheres in all compounds are comparable, as well as the intrachain magnetic interactions. However, different hydrogen-bond mediated Co...Co distances are responsible for activating/deactivating magnetic ordering in addition to the occurrence of SCM (single-chain magnet) behaviour.

Taking into account that the long-range magnetic ordering prevents us from fitting the dc magnetic data of complex 2 and estimating the zfs parameters, theoretical calculations are essential in their evaluation. In this case, the calculation gives a large negative $D = -59.4 \text{ cm}^{-1}$ along with a large rhombicity parameter ($E/D = 0.21$), which makes the sign of the main *D* parameter meaningless (see Table S7†), as discussed before for compound 1.^{55–57} In order to understand the origin of the zfs parameters in this compound, we examined the electronic configurations for the active space of the ground and lowest-lying states (see Table S10†). As expected for a severely distorted square pyramid, all d-orbitals are separated in energy and the $(d_{yz})^2(d_{xz})^2(d_{xy})^1(d_{z^2})^1(d_{x^2-y^2})^1$ configuration better represents the ground state according to the *ab initio* ligand field theory (AILFT) method (Fig. 7). It is worth noting that d_{xy} and d_{xz} orbitals cannot be distinguished and appear to be admixed between the HOMO and LUMO orbitals as a consequence of the large distortion present (Table S9†), which could explain the sign of the lowest-lying transitions involved in the zfs parameters of the compound. As observed in Table S7,† computational calculations predict negative and positive signs for the first and second excitations, which mainly represent the sign and magnitude of the *D* parameter. Therefore, according to the different $|m_l|$ values of the d_{xy} (± 2) and d_{xz}/d_{yz} (± 1) orbitals and the transition energies (Table S10†), the main $d_{xz} \rightarrow d_{xy}$

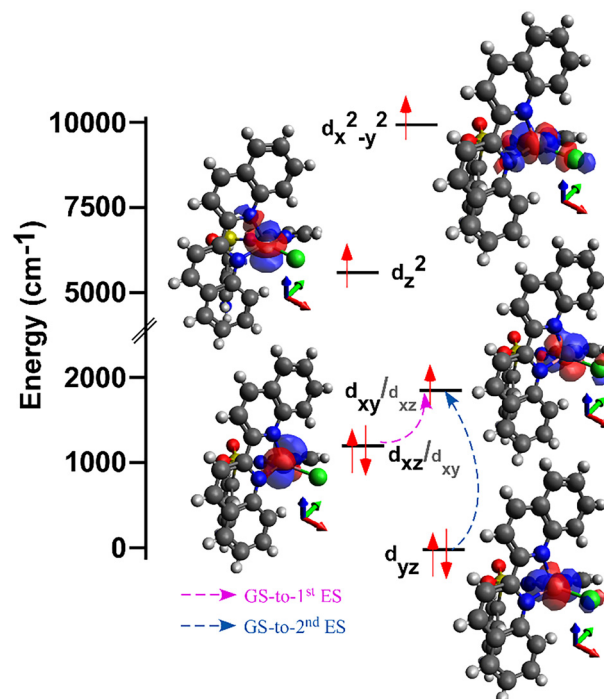


Fig. 7 NEVPT2-AILFT computed d-orbital splitting for compound 2. The dashed lines represent the first and second excitations, which contribute to the zfs parameters of the compound.

transition should govern the first transition, whereas the second one should mainly consist of the $d_{yz} \rightarrow d_{xz}$ (taking into account the minor, but still significant, contribution of d_{xz} to the third orbital) transition, which can only be explained according to the previous admixture. Moreover, such an admixture involving the d_{xy} and d_{xz} orbitals, with a predominant equatorial and axial component, respectively, could also be the origin of the large rhombicity present in the compound and the ambiguous overall sign of the zfs parameters.

In spite of the significant magnetic anisotropy present, the occurrence of zero-field SMM behaviour is not expected in the present case in view of the large value for the matrix element ($0.5\mu_B$) connecting both ground Kramers doublets (Fig. S11†), which suggests that a considerable tunnelling effect could completely quench the slow magnetic relaxation. In addition, the possible SIM behaviour in this compound would compete with the long range magnetic ordering provided by spin-canting, which is the reason for subsequent dilution attempts.

As described in the upcoming sections, the Ni(II) based counterpart 3 was synthesized in order to simulate a diamagnetic dilution of 2 because it was not possible to synthesize the isostructural Zn(II) counterpart. This unconventional strategy is based on a recently published work reported by Zadrozny and coworkers,⁶⁴ where they took advantage of the positive *D* value of the Ni(II) counterpart in $(\text{Ph}_4\text{P})_2[\text{M}(\text{SPh})_4]$ (where M is Mn(II), Fe(II), Co(II) or Ni(II) in their study) that simulates a diamagnetic ground state ($M_S = 0$). Due to the lower expected magnetic anisotropy, the $\chi_M T$ curve of 3 does



not show any canted antiferromagnetism (Fig. S12†). In fact, this curve can be properly fitted with the PHI software by using the following Hamiltonian:

$$\hat{H} = D\left(\hat{S}_z^2 - \frac{S(S+1)}{3}\right) + \mu_B H g \hat{S}_z - zJ'\langle S_z \rangle S_z \quad (3)$$

As observed in Fig. S12,† the susceptibility curve fits well for both positive and negative D values. In the first attempt, the curve was properly fitted, affording $D = +12.5(2) \text{ cm}^{-1}$, $g = 2.2(0)$ and $R = 2.2 \times 10^{-2}$, but without including the intermolecular $-zJ$ interactions. In the second attempt, we obtained a similar result with the following set of parameters: $D = -12.4(9) \text{ cm}^{-1}$, $g = 2.3(0)$ and $R = 7.1 \times 10^{-2}$, including $zJ = -0.5 \text{ cm}^{-1}$. The origin of such ambiguity is also explained by the large rhombicity present in the compound, as suggested by CAS-SCF/NEVPT2 calculations (*vide infra*, see Table S8†). Considering the short M...M distances found in the crystal structure and that intermolecular interactions govern the static and dynamic (*vide infra*) properties of the Co(II) based counterpart, both fitting procedures seem reasonable and, therefore, the ground state of **3** could be either $M_S = \pm 1$ or $M_S = 0$. Accordingly, the Ni/Co heterometallic mixture was studied to explore the possible improvement of SMM behaviour by means of the dilution of Co in a Ni based matrix.

Dynamic magnetic properties

In view of the results obtained by the theoretical calculations, which show large magnetic anisotropy in both compounds, dynamic ac magnetic measurements were carried out on both complexes at zero and optimal applied external magnetic dc fields in order to explore their SMM behaviour.

At a zero applied dc field, no signal was observed in the $\chi''_M(T)$ plot for **1**, which may be due to the existence of a fast QTM process hiding the desired SMM behaviour (Fig. S13†). In view of that, the field-dependent ac response was studied at 2 K. As observed in Fig. S14 and S15†, the SMM behaviour arises even at the lowest applied dc field of 250 Oe. Notably, the slowest relaxation time was found at 1 kOe, becoming faster at 2.5 kOe due to the enhancement of a field-induced direct process. Thus, temperature- and frequency-dependent measurements were carried out with an external field of 1 kOe (Fig. 8). Under these conditions, QTM is at least partially quenched and **1** displays temperature- and frequency-dependent maxima below 4 K. Both $\chi'_M(\chi''_M)$ or Cole–Cole plots and $\chi''_M(\nu)$ curves were fitted to the generalized Debye model within in the 2–4 K temperature range (Fig. S17 and S18†). As expected for an octahedral Co(II) complex, the relaxation of magnetization is best described by a Raman process (Fig. 8, top, inset) instead of an Orbach mechanism involving excited states. In fact, a linear fit of the Arrhenius plot involves $U_{\text{eff}} = 9.2(2) \text{ K}$ (6.4 cm^{-1}), a value that is much lower than the calculated $2D$ or the theoretically calculated energy gap between the ground and excited Kramers doublets by means of SINGLE_ANISO (244 K, 169.5 cm^{-1} ; see Fig. S10†). In fact, a single Raman mechanism well describes the temperature

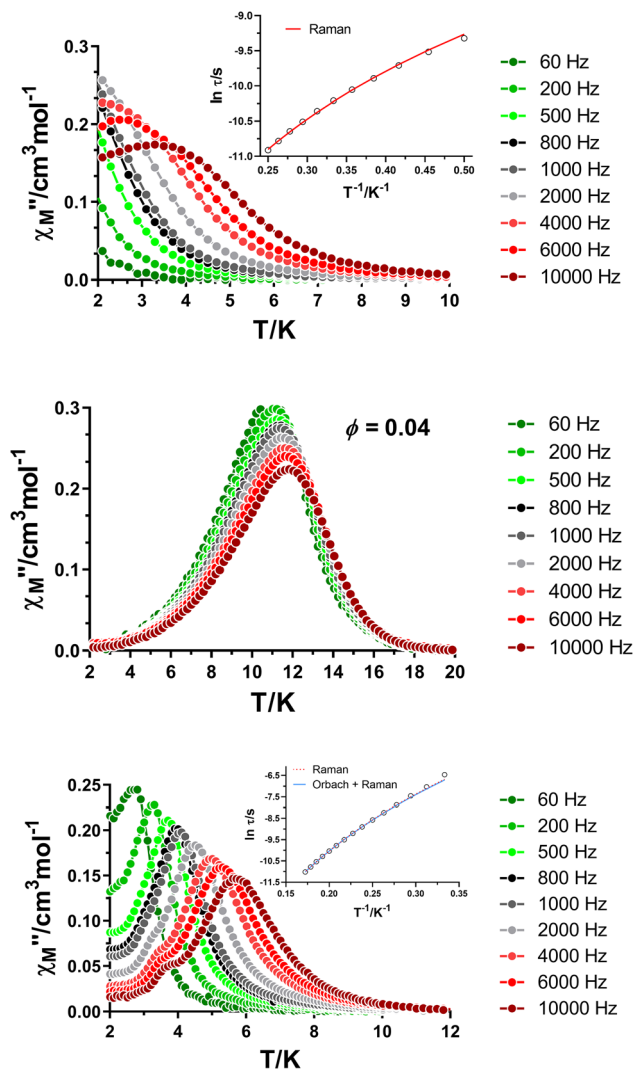


Fig. 8 Temperature dependence of the out-of-phase components of the ac susceptibility in a dc applied field of 1 kOe for **1** (top) and **2** (bottom) and in a zero applied dc field for **2** (middle). Insets: Arrhenius plots for the relaxation times considering a Raman mechanism (top and bottom).

dependence of the relaxation times, in agreement with the low α values calculated from the Cole–Cole plots (Fig. S17†). Thus, the temperature-dependence of the relaxation times was fitted to the following eqn (4):

$$\tau^{-1} = BT^n \quad (4)$$

The best fit provided B and n values of $2055(67) \text{ s}^{-1} \text{ K}^{-n}$ and $2.36(2)$, respectively. Additionally, the lack of zero-field SMM behaviour is also well explained by the matrix element within the ground state, which predicts a large tunnelling phenomenon with a value of $1.7\mu_B$ (see Fig. S10†).

In good agreement with the long-range weak ferromagnetic ordering present in **2**, the data collected at zero-field showed temperature- and frequency-independent maxima in both of the $\chi'_M(T)$ and $\chi''_M(T)$ signals (Fig. S19† and Fig. 8, middle).



The fact of having these maxima at 11 K is in good agreement with the bifurcation temperature found in the FC/ZFC measurement. In order to confirm that the maxima do not correspond to the SMM behaviour, the Mydosh parameter,⁶⁵ ϕ , was calculated using the formula $\phi = ((\Delta T_p/T_p)/\Delta \log f)$, giving a value of $\phi = 0.04$, which is consistent with a glassy state probably derived from the opposed weak ferro/antiferromagnetic interactions and not SMM behaviour.

Without discarding the possibility of a hidden SMM behaviour, field-dependent measurements were performed at 2.8 K for **2**. As depicted in Fig. S20 and S21,[†] an optimum field of 1 kOe was determined for complex **2**. Under these optimal conditions, frequency-dependent maxima were measured below 6 K within $\chi''_M(T)$ plots in agreement with a field-induced SMM behaviour. Cole–Cole and $\chi''_M(\nu)$ plots were fitted within the 3.0–5.8 K temperature range and, once again, relaxation times were fitted to a Raman mechanism. The fitting to eqn (4) provided B and n values of $0.58(2) \text{ s}^{-1} \text{ K}^{-n}$ and $6.58(2)$, respectively. However, taking into account that the α values extracted from the Cole–Cole plots are slightly larger than those calculated for **1** (Fig. S23[†]) and considering the calculated D value, we also considered the simultaneous occurrence of Orbach and Raman mechanisms using eqn (5):

$$\tau^{-1} = \tau_0^{-1} \exp(-U_{\text{eff}}/K_B T) + B T^n \quad (5)$$

Unfortunately, reasonable fitting parameters were not obtained. Before totally discarding the Orbach mechanism, we tried other attempts involving both QTM and direct processes along the Orbach relaxation pathway, but all our attempts were unsuccessful.

In view of the non-negligible Co...Co interactions appearing in **2**, we made several attempts in order to obtain the isostructural and diamagnetic Zn(II) counterpart to study the relaxation behaviour of a single [Co(SDZ)(bq)Cl] molecule in a diluted Zn-based matrix. However, no attempts involving ZnCl₂ afforded the desired compound. As an alternative route, we synthesized the Ni(II) counterpart **3**. Very recently, Zadrozny and coauthors have reported the relaxation dynamics of the (Ph₄P)₂[Co(SPh)₄] zero-field SMM diluted in different paramagnetic matrices. As they show, when the SMM is diluted in a Ni(II) matrix with $D > 0$, the $M_S = 0$ sublevel is the only populated one at low temperatures with no spin angular momentum, which simulates, somehow, a dilution in a diamagnetic matrix alternative to the use of Zn(II). In this case, the dilution favours slower relaxation times due to an effective quenching of QTM.

In our work, we have tried to mimic their strategy for our compound **2**. Hence, compound **2**_{Ni} was successfully synthesized by using a 1:10 Co:Ni ratio, showing purity and homogeneity by PXRD analysis (Fig. S2[†]). Once again, dynamic ac magnetic measurements were initially performed under a zero applied dc field. Considering that **3** does not show any measurable spin-canted effect in the $\chi_M T$ curve, we did not expect it within **2**_{Ni}. However, as clearly observed in Fig. S25 and S26,[†] this diluted analogue displays frequency-independent maxima at 6.5 K in agreement with the long-range mag-

netic ordering shown by the cobalt analogue. In view of this, and with the aim of comparing the relaxation times measured in the same experimental conditions, ac magnetic properties of **2**_{Ni} were studied under an external magnetic dc field of 1 kOe. The $\chi''_M(T)$ plots reveal field-induced SMM behaviour with maxima below 5.2 K, a slightly lower temperature than that for **2** (Fig. S28[†]). Relaxation times and α values were obtained by fitting the Cole–Cole and $\chi''_M(\nu)$ plots in the 2.0–5.2 K temperature range. As observed in Fig. 9, relaxation times for **2**_{Ni} display a larger curvature than that expected for a single Raman mechanism (dashed blue line). This is supported by the slightly larger α values obtained for this compound, which suggest the occurrence of an additional magnetic relaxation pathway. Thus, we considered the simultaneous presence of a Raman and a direct process by the following equation:

$$\tau^{-1} = B T^n + A_{\text{direct}} T \quad (6)$$

The fit afforded the following set of parameters: $B = 27(6) \text{ s}^{-1} \text{ K}^{-n}$; $n = 4.4(1)$ and $A_{\text{direct}} = 1881(120) \text{ s}^{-1} \text{ K}^{-1}$. Note that a similar fit could be obtained by replacing the direct mechanism with QTM (Fig. S31[†]). In any case, the most important conclusion is that relaxation times are faster for **2**_{Ni} than for **2** in the whole temperature regime.

It is clear that this system is not appropriate to perform the mentioned approach. Indeed, in view of the evolution of the relaxation times, we assume that the Ni(II) based counterpart must have a non-desired negative D value with $M_S = \pm 1$ as the ground state. *Ab initio* calculations based on an optimized nickel-based model give $D = -21.5 \text{ cm}^{-1}$ although the negative sign is, again, not meaningful in view of the large rhombicity ($E/D = 0.22$, see Table S8[†]). Consequently, these results could explain why the relaxation times are not slowed down in this case because, although those few [Co(SDZ)(bq)Cl] complexes were aimed to be surrounded by either completely diamagnetic (with Zn(II)) or somewhat diamagnetic ions at low temperatures (Ni(II) with $D > 0$), they possess neighbouring paramag-

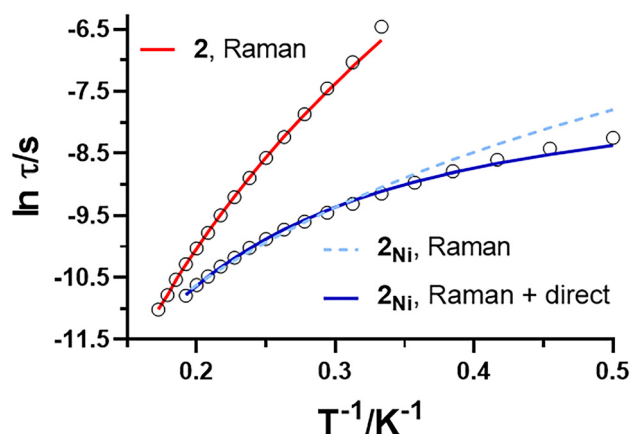


Fig. 9 Comparison of the Arrhenius plots for the relaxation times obtained for compounds **2** (red) and **2**_{Ni} (blue) measured under the same experimental conditions.



netic molecules. In this sense, it is worth mentioning that the system that we have studied in this work and $(\text{Ph}_4\text{P})_2[\text{Co}(\text{SPh})_4]$ display notable differences. On the one hand, in the previously reported case, the paramagnetic centres within the crystal structure are much farther from each other and no sizeable interaction is observed. In our case, instead, the short Co...Co distances appeared to be fundamental when explaining the magnetic properties. On the other hand, $(\text{Ph}_4\text{P})_2[\text{Co}(\text{SPh})_4]$ behaves as a zero-field SMM, while in our case an external magnetic field needs to be applied to observe slow relaxation of magnetization.

Conclusions

We have successfully synthesized and characterized two novel Co(II) based mononuclear compounds based on SDZ and additional chelating phen and bq ligands named **1** (phen) and **2** (bq). Moreover, the isostructural Ni(II) analogue of **2** has been prepared for further magnetic studies. As predicted, the coordination spheres differ from one to another due to the bulky character of bq, having CoN_6 and CoN_4Cl spheres for **1** and **2**, respectively. Consequently, both compounds share sizeable magnetic anisotropy characterized by significant rhombicity as suggested by experimental magnetic studies and theoretical calculations. The negative (although meaningless) sign of the calculated D parameter in **2** is probably due to an admixture involving d_{xy} and d_{xz} orbitals, which could also be the origin of the large rhombicity present in the compound. As reported for other octahedral Co(II) based magnets, **1** behaves as a field-induced SMM with the magnetization relaxation mechanism based on a Raman process. In contrast, complex **2** displays spin-canted antiferromagnetism that, perhaps, hides slow magnetic relaxation at zero applied dc field. Under an optimal external magnetic field, field-induced SMM behaviour arises with a relaxation process governed by a Raman mechanism. In view of the unsuccessful preparation of the Zn(II) counterpart of **2**, $[\text{Co}(\text{SDZ})(\text{bq})\text{Cl}]$ was diluted in a Ni(II) matrix, yielding compound **2**_{Ni}. This new compound still displays spin-canted antiferromagnetism and, therefore, the potential zero-field SMM behaviour did not emerge in this material. In addition, the relaxation rates appear to be even faster than those of the pure compound **2**, evidencing a paramagnetic ground-state for the Ni(II) counterpart, also demonstrated by theoretical calculations. Further work is in progress to study other paramagnetic dilutions with the aim of understanding the differences that might appear by carrying out dilutions with other metal ions. Moreover, solution studies of **2** would also be interesting in order to confirm or deny the potential zero-field SMM behaviour of $[\text{Co}(\text{SDZ})(\text{bq})\text{Cl}]$.

Conflicts of interest

There are no conflicts to declare.

Acknowledgements

C. V.-P. acknowledges the financial support from ANPCYT (PICT 2019-02589). D. B. S. and G. A. E. would like to thank Universidad Nacional de La Plata (UNLP) 11X/876 and X857 and CONICET. The financial support by Gobierno Vasco/Eusko Jaurlaritza (IT1755-22) is also acknowledged. The authors are thankful for the technical and human support provided by the Geochronology and Isotope Geochemistry-SGIker facility of UPV/EHU and European funding (ERDF and ESF). The authors acknowledge Dr María Mar Quesada-Moreno for insightful discussions and help with the quantum-chemical calculations, and they are also grateful to Dr Oscar Castillo for the enlightening discussions on the magnetic properties of these compounds.

References

- 1 R. Sessoli, D. Gatteschi, A. Caneschi and M. A. Novak, *Nature*, 1993, **365**, 141–143.
- 2 F. Neese and D. A. Pantazis, *Faraday Discuss.*, 2011, **148**, 229–238.
- 3 N. Ishikawa, M. Sugita, T. Ishikawa, S. Y. Koshihara and Y. Kaizu, *J. Am. Chem. Soc.*, 2003, **125**, 8694–8695.
- 4 A. Zabala-Lekuona, J. M. Seco and E. Colacio, *Coord. Chem. Rev.*, 2021, **441**, 213984.
- 5 J. Su, L. Yin, Z. Ouyang, Z. Wang and W. Zheng, *Dalton Trans.*, 2020, **49**, 6945–6949.
- 6 A. Cornia, A. L. Barra, V. Bulicanu, R. Clérac, M. Cortijo, E. A. Hillard, R. Galavotti, A. Lunghi, A. Nicolini, M. Rouzières, L. Sorace and F. Totti, *Inorg. Chem.*, 2020, **59**, 1763–1777.
- 7 N. I. Gumerova, A. Roller, G. Giester, J. Krzystek, J. Cano and A. Rompel, *J. Am. Chem. Soc.*, 2020, **142**, 3336–3339.
- 8 R. C. Poulten, M. J. Page, A. G. Algarra, J. J. Le Roy, I. López, E. Carter, A. Llobet, S. A. Macgregor, M. F. Mahon, D. M. Murphy, M. Murugesu and M. K. Whittlesey, *J. Am. Chem. Soc.*, 2013, **135**, 13640–13643.
- 9 J. Miklovič, D. Valigura, R. Boča and J. Titiš, *Dalton Trans.*, 2015, **44**, 12484–12487.
- 10 K. E. R. Marriott, L. Bhaskaran, C. Wilson, M. Medarde, S. T. Ochsenbein, S. Hill and M. Murrie, *Chem. Sci.*, 2015, **6**, 6823–6828.
- 11 J. M. Zadrozny, D. J. Xiao, M. Atanasov, G. J. Long, F. Grandjean, F. Neese and J. R. Long, *Nat. Chem.*, 2013, **5**, 577–581.
- 12 J. M. Zadrozny, M. Atanasov, A. M. Bryan, C. Y. Lin, B. D. Reinken, P. P. Power, F. Neese and J. R. Long, *Chem. Sci.*, 2013, **4**, 125–138.
- 13 J. M. Zadrozny and J. R. Long, *J. Am. Chem. Soc.*, 2011, **133**, 20732–20734.
- 14 T. Jurca, A. Farghal, P. H. Lin, I. Korobkov, M. Murugesu and D. S. Richeson, *J. Am. Chem. Soc.*, 2011, **133**, 15814–15817.



- 15 J. Vallejo, A. Pascual-Álvarez, J. Cano, I. Castro, M. Julve, F. Lloret, J. Krzystek, G. De Munno, D. Armentano, W. Wernsdorfer, R. Ruiz-García and E. Pardo, *Angew. Chem., Int. Ed.*, 2013, **52**, 14075–14079.
- 16 R. Ishikawa, R. Miyamoto, H. Nojiri, B. K. Breedlove and M. Yamashita, *Inorg. Chem.*, 2013, **52**, 8300–8302.
- 17 X. N. Yao, J. Z. Du, Y. Q. Zhang, X. B. Leng, M. W. Yang, S. Da Jiang, Z. X. Wang, Z. W. Ouyang, L. Deng, B. W. Wang and S. Gao, *J. Am. Chem. Soc.*, 2017, **139**, 373–380.
- 18 P. C. Bunting, M. Atanasov, E. Damgaard-Møller, M. Perfetti, I. Crassee, M. Orlita, J. Overgaard, J. Van Slageren, F. Neese and J. R. Long, *Science*, 2018, **362**, 7319.
- 19 J. M. Frost, K. L. M. Harriman and M. Murugesu, *Chem. Sci.*, 2016, **7**, 2470–2491.
- 20 G. A. Craig and M. Murrie, *Chem. Soc. Rev.*, 2015, **44**, 2135–2147.
- 21 Y. F. Deng, T. Han, Z. Wang, Z. Ouyang, B. Yin, Z. Zheng, J. Krzystek and Y. Z. Zheng, *Chem. Commun.*, 2015, **51**, 17688–17691.
- 22 C. Villa-Pérez, I. Oyarzabal, G. A. Echeverría, G. C. Valencia-Urbe, J. M. Seco and D. B. Soria, *Eur. J. Inorg. Chem.*, 2016, 4835–4841.
- 23 M. Feng and M. L. Tong, *Chem. – Eur. J.*, 2018, **24**, 7574–7594.
- 24 X. X. Jin, X. X. Chen, J. Xiang, Y. Z. Chen, L. H. Jia, B. W. Wang, S. C. Cheng, X. Zhou, C. F. Leung and S. Gao, *Inorg. Chem.*, 2018, **57**, 3761–3774.
- 25 L. Chen, J. Wang, J.-M. Wei, W. Wernsdorfer, X.-T. Chen, Y.-Q. Zhang, Y. Song and Z.-L. Xue, *J. Am. Chem. Soc.*, 2014, **136**, 12213–12216.
- 26 L. Chen, S. Y. Chen, Y. C. Sun, Y. M. Guo, L. Yu, X. T. Chen, Z. Wang, Z. W. Ouyang, Y. Song and Z. L. Xue, *Dalton Trans.*, 2015, **44**, 11482–11490.
- 27 A. Sarkar, S. Dey and G. Rajaraman, *Chem. – Eur. J.*, 2020, **26**, 14036–14058.
- 28 J. B. Tommasino, F. N. R. Renaud, D. Luneau and G. Pilet, *Polyhedron*, 2011, **30**, 1663–1670.
- 29 O. Pajuelo-Corral, A. Zabala-Lekuona, E. San Sebastian, A. Rodríguez-Diéguez, J. A. García, L. Lezama, E. Colacio, J. M. Seco and J. Cepeda, *Chem. – Eur. J.*, 2020, **26**, 13484–13498.
- 30 S. Titos-Padilla, J. Ruiz, J. M. Herrera, E. K. Brechin, W. Wernsdorfer, F. Lloret and E. Colacio, *Inorg. Chem.*, 2013, **52**, 9620–9626.
- 31 S. G. de Madinabeitia, M. E. S. Lorda and J. I. G. Ibarguchi, *Anal. Chim. Acta*, 2008, **625**, 117–130.
- 32 CrysAlis CCD (Computer Software), CrysAlis RED and associated programs: Oxford Diffraction program, Oxford Diffraction Ltd, Abingdon, England, 2006.
- 33 G. M. Sheldrick, *SHELXS-97. Program for Crystal Structure Resolution*, University of Göttingen, Göttingen, Germany, 1997.
- 34 G. M. Sheldrick, *SHELXL-97. Program for Crystal Structure Analysis*, University of Göttingen, Göttingen, Germany, 1997.
- 35 M. J. Frisch, G. W. Trucks, H. B. Schlegel, G. E. Scuseria, M. A. Robb, J. R. Cheeseman, G. Scalmani, V. Barone, G. A. Petersson, H. Nakatsuji, X. Li, M. Caricato, A. V. Marenich, J. Bloino, B. G. Janesko, R. Gomperts, B. Mennucci, H. P. Hratchian, J. V. Ortiz, A. F. Izmaylov, J. L. Sonnenberg, D. Williams-Young, F. Ding, F. Lipparini, F. Egidi, J. Goings, B. Peng, A. Petrone, T. Henderson, D. Ranasinghe, V. G. Zakrzewski, J. Gao, N. Rega, G. Zheng, W. Liang, M. Hada, M. Ehara, K. Toyota, R. Fukuda, J. Hasegawa, M. Ishida, T. Nakajima, Y. Honda, O. Kitao, H. Nakai, T. Vreven, K. Throssell, J. A. Jr., J. E. Peralta, F. Ogliaro, M. J. Bearpark, J. J. Heyd, E. N. Brothers, K. N. Kudin, V. N. Staroverov, T. A. Keith, R. Kobayashi, J. Normand, K. Raghavachari, A. P. Rendell, J. C. Burant, S. S. Iyengar, J. Tomasi, M. Cossi, J. M. Millam, M. Klene, C. Adamo, R. Cammi, J. W. Ochterski, R. L. Martin, K. Morokuma, O. Farkas, J. B. Foresman and D. J. Fox, *Gaussian 16*, Revision A.03, Gaussian, Inc., Wallingford CT, 2016..
- 36 A. D. Becke, *Phys. Rev. A*, 1988, **38**, 3098–3100.
- 37 A. Schäfer, H. Horn and R. Ahlrichs, *J. Chem. Phys.*, 1992, **97**, 2571–2577.
- 38 V. A. Rassolov, J. A. Pople, M. A. Ratner and T. L. Windus, *J. Chem. Phys.*, 1998, **109**, 1223–1229.
- 39 F. Neese, F. Wennmohs, U. Becker and C. Riplinger, *J. Chem. Phys.*, 2020, **152**, 224108.
- 40 F. Neese, *Wiley Interdiscip. Rev.: Comput. Mol. Sci.*, 2012, **2**, 73–78.
- 41 C. Lee, W. Yang and R. G. Parr, *Phys. Rev. B: Condens. Matter Mater. Phys.*, 1988, **37**, 785–789.
- 42 A. D. Becke, *J. Chem. Phys.*, 1993, **98**, 5648–5652.
- 43 C. van Wüllen, *J. Chem. Phys.*, 1998, **109**, 392–399.
- 44 F. Weigend and R. Ahlrichs, *Phys. Chem. Chem. Phys.*, 2005, **7**, 3297–3305.
- 45 F. Weigend, *Phys. Chem. Chem. Phys.*, 2006, **8**, 1057–1065.
- 46 A. Hellweg, C. Hättig, S. Höfener and W. Klopper, *Theor. Chem. Acc.*, 2007, **117**, 587–597.
- 47 Y. F. Deng, M. K. Singh, D. Gan, T. Xiao, Y. Wang, S. Liu, Z. Wang, Z. Ouyang, Y. Z. Zhang and K. R. Dunbar, *Inorg. Chem.*, 2020, **59**, 7622–7630.
- 48 C. Angeli, S. Borini, M. Cestari and R. Cimiraglia, *J. Chem. Phys.*, 2004, **121**, 4043–4049.
- 49 D. Maganas, S. Sottini, P. Kyritsis, E. J. J. Groenen and F. Neese, *Inorg. Chem.*, 2011, **50**, 8741–8754.
- 50 M. Llunell, D. Casanova, J. Cirera, J. M. Bofill, P. Alemany, S. Alvarez, M. Pinsky and D. Avnir, *SHAPE (Computer Software)*, Barcelona, 2005.
- 51 J. E. Campbell, J. Yang and G. M. Day, *J. Mater. Chem. C*, 2017, **5**, 7574–7584.
- 52 A. Guijarro, J. A. Vergés, E. San-Fabián, G. Chiappe and E. Louis, *ChemPhysChem*, 2016, **17**, 3548–3557.
- 53 R. Boča, C. Rajnák and J. Titiš, *Magnetochemistry*, 2023, **9**, 100.
- 54 N. F. Chilton, R. P. Anderson, L. D. Turner, A. Soncini and K. S. Murray, *J. Comput. Chem.*, 2013, **34**, 1164–1175.
- 55 M. Atanasov, D. Aravena, E. Suturina, E. Bill, D. Maganas and F. Neese, *Coord. Chem. Rev.*, 2015, **289–290**, 177–214.
- 56 J. Cirera, E. Ruiz, S. Alvarez, F. Neese and J. Kortus, *Chem. – Eur. J.*, 2009, **15**, 4078–4087.



- 57 D. Maganas, J. Krzystek, E. Ferentinos, A. M. Whyte, N. Robertson, V. Psycharis, A. Terzis, F. Neese and P. Kyritsis, *Inorg. Chem.*, 2012, **51**, 7218–7231.
- 58 R. Herchel, L. Váhovská, I. Potočník and Z. Trávníček, *Inorg. Chem.*, 2014, **53**, 5896–5898.
- 59 E. Colacio, J. Ruiz, E. Ruiz, E. Cremades, J. Krzystek, S. Carretta, J. Cano, T. Guidi, W. Wernsdorfer and E. K. Brechin, *Angew. Chem., Int. Ed.*, 2013, **52**, 9130–9134.
- 60 M. Fumanal, J. Jornet-Somoza, S. Vela, J. J. Novoa, J. Ribas-Arino and M. Deumal, *J. Mater. Chem. C*, 2021, **9**, 10647–10660.
- 61 Y. H. Chi, L. Yu, J. M. Shi, Y. Q. Zhang, T. Q. Hu, G. Q. Zhang, W. Shi and P. Cheng, *Dalton Trans.*, 2011, **40**, 1453–1462.
- 62 C. Hou, J. M. Shi, Y. M. Sun, W. Shi, P. Cheng and L. D. Liu, *Dalton Trans.*, 2008, 5970–5976.
- 63 Y. Zhang, Z. Y. Liu, H. M. Tang, B. Ding, Z. Y. Liu, X. G. Wang, X. J. Zhao and E. C. Yang, *Inorg. Chem. Front.*, 2022, **9**, 5039–5047.
- 64 I. P. Moseley, C. P. Ard, J. A. DiVerdi, A. Ozarowski, H. Chen and J. M. Zadrozny, *Cell Rep. Phys. Sci.*, 2022, **3**, 100802.
- 65 J. A. Mydosh, *Spin Glasses*, Taylor & Francis, Washington, DC, 1993.

